Information Processing Letters 137 (2018) 26–32

Contents lists available at ScienceDirect

Information Processing Letters

www.elsevier.com/locate/ipl

Perona–Malik model with self-adjusting shape-defining constant

Baraka Maiseli [a,*], Hubert Msuya [a], Suzan Kessy [b], Michael Kisangiri [b]

[a] Department of Electronics & Telecommunications Engineering, College of Information & Communication Technologies, University of Dar es Salaam, P.O. Box 33335, Dar es Salaam, Tanzania

[b] Department of Communication Science & Engineering, School of Computational & Communication Science & Engineering, Nelson Mandela African Institute of Science & Technology, P.O. Box 447, Arusha, Tanzania

ARTICLE INFO

Article history:
Received 9 February 2017
Received in revised form 23 April 2018
Accepted 30 April 2018
Available online 2 May 2018
Communicated by Jinhui Xu

Keywords:
Algorithms
Noise removal
Denoising
Diffusion

ABSTRACT

For decades, the Perona–Malik (PM) diffusion model has been receiving a considerable attention of scholars for its ability to restore detailed scenes. The model, despite its promising results, demands manual tuning of the shape-defining constant—a process that consumes time, prompts for human intervention, and limits flexibility of the model in real-time systems. Most works have tried to address other weaknesses of the PM model (non-convexity and non-monotonicity, which produce chances for instability and multiple solutions), but automating PM remains an open-ended question. In this work, we have introduced a new implementation approach that fully automates the PM model. In particular, the tuning parameters have been conditioned to ensure that the model guarantees convergence and is entirely convex over the scale-space domain. Experiments show that our implementation strategy is flexible, automatic, and achieves convincing results.

1. Introduction

Humans are naturally inclined to visually appealing scenes for they reveal more details, thus making them easier to interpret and analyze. In medical applications, such as in magnetic resonance induction (MRI), for example, doctors prefer uncorrupted MRI images to provide proper treatments to patients. Despite this important demand, most scenes suffer from noise and other unwanted artifacts, which are partly due to acquisition systems (like diffraction limits and point spread function of lenses) and interferences from external environments. Therefore, extensive works on image restoration—denoising [1–11], enhancement [12–15], super-resolution [16–28], and inpainting [29–34], to mention a few—have been conducted to restore original scenes from their degraded versions. This work deals with the image denoising problem.

Methods to solve the image denoising problem can majorly be grouped into three: (1) linear and nonlinear diffusion-based [11], (2) Total Variation or TV [10,35–37], and (3) Wavelet-based [38–41]. Of these groups, nonlinear diffusion-steered approaches—inspired by a novel and an interesting work of Perona and Malik [11]—have attracted attention of most scholars due to the ability of these approaches to denoise scenes while retaining critical features [5,42–44]. We, therefore, have laid the foundation of our work on the Perona–Malik (PM) model.

In the PM diffusion model, noise removal in the image is engineered in a discriminatory fashion through a well-crafted diffusion coefficient. The regularization kernel associated with the PM equation is stronger in intra-region and weaker in inter-region, a phenomenon that simulta-

* Corresponding author.
E-mail address: barakamaiseli@yahoo.com (B. Maiseli).

https://doi.org/10.1016/j.ipl.2018.04.016
0020-0190/

neously suppresses noise and encourages edge recovery. The major weakness of the PM model, as noted by several authors, is that it tends to introduce speckle noise and staircasing effects into the final results [9,1,45,46]. Perhaps the problem is due to the non-convex nature of the PM potential. Another potential drawback of the Perona–Malik model revolves in the shape-defining parameter of the diffusion coefficient. In [11], authors suggest two approaches to determine the value of the shape-defining parameter: (1) tuning manually, which is inconvenient and time consuming, and (2) applying the "noise estimator" proposed by Canny [47], which requires noise statistics of an image. In this work, we have developed a strategy to automatically and adaptively update the shape-defining parameter—even without requiring prior knowledge on image noise—while conditioning the PM potential within a convex region. Consequently, the minimization process is guaranteed to converge to a unique solution.

2. Nonlinear diffusion processes

2.1. What is diffusion in digital images?

Diffusion, as applied to digital images, involves the process where low-value pixels receive weight from high-value ones without modifying the total pixel count [48]. Indeed, the phenomenon defines a noise removal process that can be intuitively cast by the *Fick's first law*

$$j = -\phi \cdot \nabla u, \tag{2.1}$$

which reflects the equilibration property: intensity gradient, ∇u, produces flux, j, which intends to compensate it at a speed controlled by the diffusion coefficient, ϕ. Substituting (2.1) into the continuity equation

$$\frac{\partial u}{\partial t} = -\text{div}\, j, \tag{2.2}$$

which accounts for the constant pixel count at any instant of the diffusion process, we get

$$\frac{\partial u}{\partial t} = \text{div}(\phi \cdot \nabla u). \tag{2.3}$$

When ϕ is independent of u, diffusion is called linear isotropic, which is analogous to the heat equation that suffers from inability to locate edge regions. To address the challenge, Perona and Malik suggested that ϕ be made a function of the evolving image, u, as in

$$\frac{\partial u}{\partial t} = \text{div}(\phi(|\nabla u|) \cdot \nabla u). \tag{2.4}$$

2.2. Traditional Perona–Malik model

To avoid smoothing "semantically useful" features, such as edges and contours, Perona and Malik proposed two spatially varying diffusion kernels:

$$\phi_1(s) = \frac{1}{1 + \left(\frac{s}{K}\right)^2} \tag{2.5}$$

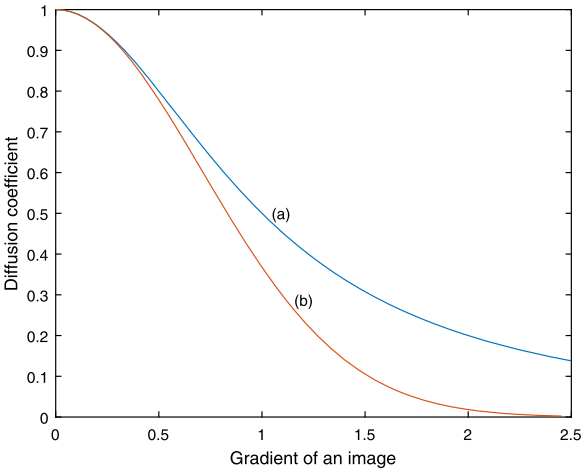

Fig. 1. Perona–Malik diffusion coefficients with shape-defining constant, $K = 1$: (a) $\phi_1(s) = \frac{1}{1+(\frac{s}{K})^2}$, and (b) $\phi_2(s) = \exp(-(s/K)^2)$.

and

$$\phi_2(s) = \exp(-(s/K)^2), \tag{2.6}$$

where $s = |\nabla u|$ and K is the shape-defining constant. Both kernels, ϕ_1 and ϕ_2, share the same properties: they evaluate to one in flat regions ($s \to 0$) and zero near potential features ($s \to \infty$), as depicted in Fig. 1. Replacing ϕ in (2.4) by ϕ_1 defined in (2.5), for instance, and incorporating a regularizing term, we get the evolution equation

$$\frac{\partial u}{\partial t} = \text{div}\left(\frac{1}{1 + \left(\frac{|\nabla u|}{K}\right)^2} \nabla u\right) - \lambda(u - f), \tag{2.7}$$

$$(x, t) \in \Omega \times (0, T), \tag{2.8}$$

$$u(x, 0) = f, \tag{2.9}$$

$$\frac{\partial u}{\partial \vec{n}} = 0, (x, t)\partial\Omega \times (0, T). \tag{2.10}$$

Ω is the supporting domain of u, λ is the tuning parameter that establishes a trade-off between the denoising image, u, and the noisy image f. The current study aims at ensuring that the optimal value of u is computed automatically in the iteration process.

2.3. Automated Perona–Malik model

Our goal was to evolve the PM model under minimum human intervention. Recalling the PM formulation in (2.7), we see that the key parameters that require manual tuning are K and λ. Now, considering the PM diffusion kernel in (2.7), we form the energy integral functional

$$\rho(s) = \int_{\Omega} \frac{s}{1 + \left(\frac{s}{K}\right)^2} dx. \tag{2.11}$$

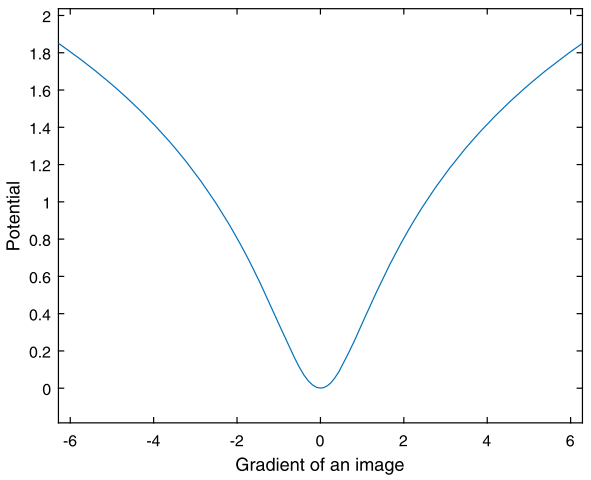

Fig. 2. Energy functional of the Perona–Malik model.

Integrating (2.11) yields the PM potential

$$\rho(s) = \frac{K^2}{2}\log\left(1+\left(\frac{s}{K}\right)^2\right), \tag{2.12}$$

which is non-convex for particular values of K (Fig. 2).

Theorem 1. *$\rho(s)$ is strictly convex if it passes the second derivative test. That is, if $\rho'' > 0\ \forall s$.*

Proof. From Theorem 1,

$$\rho''(s) = \frac{1}{1+\left(\frac{s}{K}\right)^2} - \frac{2s^2}{K^2\left(1+\left(\frac{s}{K}\right)^2\right)^2}, \tag{2.13}$$

and the condition for $\rho(s)$ to be strictly convex is that

$$\frac{1}{1+\left(\frac{s}{K}\right)^2} > \frac{2s^2}{K^2\left(1+\left(\frac{s}{K}\right)^2\right)^2},$$

which reduces to $K > s$.

Without loss of generality, we implemented the convexity condition in the computer as

$$K = \delta + s^{\alpha}, \tag{2.14}$$

which still satisfies the condition, $K > s$, for $\delta > 0$ and $0 < \alpha \leq 1$. In the practical implementation of the model, we found optimal values of δ and α as 1 and 0.5, respectively. Therefore, the new shape-defining parameter becomes

$$K = 1 + \sqrt{s}, \tag{2.15}$$

Additionally, λ is automated by first considering optimal conditions in (2.7); that is, as $t \to \infty$, $\frac{\partial u}{\partial t} \approx 0$ and u becomes the minimizer of the optimization problem in (2.12). Therefore, establishing steady states in (2.7) and multiplying both sides of the resulting equation by $(u-f)$, we get

$$0 = (u-f)\left[\operatorname{div}\left(\frac{1}{1+\left(\frac{|\nabla u|}{K}\right)^2}\nabla u\right)\right] - \lambda(u-f)^2. \tag{2.16}$$

Rearranging (2.16), subjecting λ, and integrating over Ω both sides of the equation, we get

$$\lambda = \frac{\int_{\Omega}(u-f)\left[\operatorname{div}\left(\frac{1}{1+\left(\frac{|\nabla u|}{K}\right)^2}\nabla u\right)\right]dx}{\int_{\Omega}(u-f)^2 dx}. \tag{2.17}$$

Next, assume that some prior knowledge about mean and variance of noise, η, (say, additive white Gaussian) is known, and defined as

$$\frac{1}{|\Omega|}\int_{\Omega}\eta dx = 0 \text{ and}$$
$$\frac{1}{|\Omega|}\int_{\Omega}\eta^2 dx = \nu^2, \tag{2.18}$$

where $\eta = (u-f)$ is the standard deviation of noise. Combining (2.16) and (2.18), then manipulating the variables to subject λ, we get

$$\lambda = \frac{1}{|\Omega|\nu^2}\int_{\Omega}(u-f)\left[\operatorname{div}\left(\frac{1}{1+\left(\frac{|\nabla u|}{K}\right)^2}\nabla u\right)\right]dx. \tag{2.19}$$

Remark 1. In this work, we have considered the additive white Gaussian noise ($f = u + \eta$). For the multiplicative noise ($f = u\eta$), such as that observed in hyperspectral and ultrasound images, however, the assumptions for mean and standard deviation of noise are

$$\frac{1}{|\Omega|}\int_{\Omega}\eta dx = 1 \text{ and}$$
$$\frac{1}{|\Omega|}\int_{\Omega}(\eta-1)^2 dx = \nu^2, \tag{2.20}$$

and the evolution equation for denoising u is

$$\frac{\partial u}{\partial t} = \operatorname{div}\left(\frac{1}{1+\left(\frac{|\nabla u|}{K}\right)^2}\nabla u\right) - \lambda\left(1-\frac{f}{u}\right), \tag{2.21}$$

$$(x,t) \in \Omega \times (0,T), \tag{2.22}$$

$$u(x,0) = f, \tag{2.23}$$

$$\frac{\partial u}{\partial \vec{n}} = 0,\ (x,t)\partial\Omega \times (0,T). \tag{2.24}$$

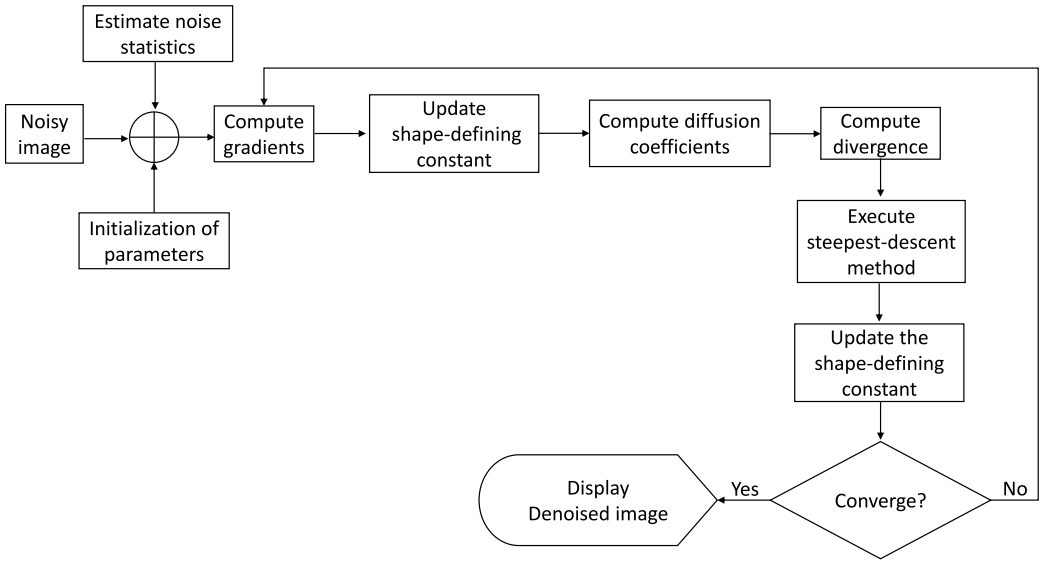

Fig. 3. Automated Perona–Malik denoising method.

Remark 2. From (2.21), and using a similar derivation strategy for the adaptive parameter, λ, we get

$$\lambda = \frac{1}{|\Omega|\nu^2}\int_{\Omega}\left(1-\frac{f}{u}\right)\left[\operatorname{div}\left(\frac{1}{1+\left(\frac{|\nabla u|}{K}\right)^2}\nabla u\right)\right]dx. \tag{2.25}$$

2.4. Numerical implementation of the proposed method

We implemented the proposed approach using four-point neighborhood explicit numerical scheme, which offers intuitive implementation strategies, promising accuracy, and guaranteed stability under the Courant–Friedrichs–Lewy (CFL) condition [49]. Therefore, consider gradients of the discretized version of u, namely $\Delta_N u_{i,j} = u_{i,j+1} - u_{i,j}$, $\Delta_S u_{i,j} = u_{i,j-1} - u_{i,j}$, $\Delta_E u_{i,j} = u_{i+1,j} - u_{i,j}$, and $\Delta_W u_{i,j} = u_{i-1,j} - u_{i,j}$, in the four directions of the scheme; the corresponding conduction coefficients are

$$cN = \frac{1}{1+\left(\frac{\Delta_N u_{i,j}}{K_{i,j}}\right)^2},\quad cS = \frac{1}{1+\left(\frac{\Delta_S u_{i,j}}{K_{i,j}}\right)^2},$$
$$cE = \frac{1}{1+\left(\frac{\Delta_E u_{i,j}}{K_{i,j}}\right)^2},\quad cW = \frac{1}{1+\left(\frac{\Delta_W u_{i,j}}{K_{i,j}}\right)^2},$$

where

$$K_{i,j} = 1 + \frac{1}{4}\sqrt{\Delta_N u_{i,j} + \Delta_S u_{i,j} + \Delta_E u_{i,j} + \Delta_W u_{i,j}}. \tag{2.26}$$

Note that the constant $\frac{1}{4}$ in (2.26) averages gradients of the scheme. The regularization parameter, λ, is computed as

$$\lambda = \frac{1}{MN\sigma^2}\sum_{i=1}^{M}\sum_{j=1}^{N}(u_{i,j} - f_{i,j})\Theta_{i,j}, \tag{2.27}$$

where σ^2 is the variance of noise, M and N are, respectively, the horizontal and vertical dimensions of $u_{i,j}$, and $\Theta_{i,j}$ represents the divergence component, which is defined by the formula

$$\Theta_{i,j} = \Delta_N u_{i,j} \times cN + \Delta_S u_{i,j} \times cS + \Delta_E u_{i,j} \times cE + \Delta_W u_{i,j} \times cW, \tag{2.28}$$

where cN, cS, cE, and cW are the conduction coefficients (discrete diffusivities) in the North, South, East, and West directions of the numerical scheme. Finally, our steepest-descent method that iteratively denoises u is

$$u_{i,j}^{(n+1)} = u_{i,j}^{(n)} + \tau(\Theta_{i,j}^{(n)} - \lambda(u_{i,j}^{(n)} - f_{i,j}^{(n)})), \tag{2.29}$$

for $0 < \tau \leq 0.25$ defined according to the CFL criterion. Fig. 3 shows the flow chart that we used to implement our formulation.

2.5. Performance evaluation indices

To quantify quality of results from different denoising methods, we applied two performance indices, namely Peak signal to noise ratio (PSNR) [50] and Structural similarity (SSIM) [51]. PSNR—possibly the oldest quality evaluation metric—defined by

$$\text{PSNR} = 10\log_{10}\left(\frac{255^2 MN}{\|u-f\|_2^2}\right), \tag{2.30}$$

quantifies the signal strength of an image relative to noise. Larger value of PSNR signifies higher signal strength, and hence higher quality. Degraded images often produce lower PSNR values. Scholars have, however, highlighted a

Fig. 4. Results of denoising methods.

major weakness of the PSNR metric that if fails to address the human vision system (HVS) [51]. Thus, an appealing image may yield lower PSNR value, and vice versa. In 2004, Wang et al. proposed an alternative performance evaluation metric

$$\text{SSIM} = \frac{(2\mu_u\mu_f + \alpha)(2\sigma_{uf} + \beta)}{(\mu_u^2 + \mu_f^2 + \alpha)(\sigma_u^2 + \sigma_f^2 + \beta)}, \tag{2.31}$$

which emulates the HVS. In (2.31), the means, variances, and covariance of u and f are respectively: μ_u, μ_f; σ_u^2, σ_f^2; and σ_{uf}. And, α and β are tuning parameters. SSIM is bounded between zero and one, and higher value implies that the test image is perceptually appealing.

3. Results and discussions

Several experiments were conducted to test the effectiveness and performance of the proposed method with

Table 1
Peak signal to noise ratio (PSNR) measurements.

Image	PSNR			
	Wicket	Guo	Perona–Malik	Our Model
Elephant	29.32	27.09	30.18	30.24
Peppers	29.61	27.38	30.62	30.71
Zelda	27.64	29.96	31.05	31.14
Cameraman	26.36	25.90	29.01	29.39
Lena	29.40	28.07	30.89	30.89
House	27.81	27.66	32.41	32.71
Building	27.81	26.78	28.09	28.12
Journey	23.82	24.16	26.13	26.21
Bridge	27.80	28.98	29.73	30.02

Table 2
Structural similarity (SSIM) measurements.

Image	SSIM			
	Wicket	Guo	Perona–Malik	Our Model
Elephant	0.7205	0.7099	0.7568	0.7591
Peppers	0.7952	0.7929	0.8187	0.8230
Zelda	0.8212	0.8565	0.8841	0.8905
Cameraman	0.7798	0.7828	0.8243	0.8475
Lena	0.8928	0.8693	0.8958	0.8997
House	0.7930	0.8279	0.8856	0.9003
Building	0.3481	0.7754	0.8118	0.8189
Journey	0.7758	0.7682	0.8260	0.8307
Bridge	07525	0.7428	0.7899	0.8101

respect to the classical methods. The experimental procedures were as follows: additive white Gaussian noise of standard deviation 30 was added to different types of images. Next, we applied our method and three other classical methods, namely Guo [1], Weickert [48], and PM [11], to the noisy images. Performance of the methods was evaluated both qualitatively and quantitatively.

Visual results demonstrate that our method removes noise more effectively and generates sharper edges. Additionally, the new approach leaves flat regions smoother and cleaner (fewer visible artifacts). This promising achievement may be attributed to the guaranteed convexity of the potential, a property that ensures anomalous issues in the evolution process are captured and corrected accordingly. With the self-regulating adaptive parameter, K, the dynamical system is conditioned to converge faster and more reliably. On the contrary, other denoising methods, which demand a user to manually adjust K, produce unsatisfactory results. For example, Weickert approach yields visible speckle noise and, for particular types of images, removes important structures (Fig. 4).

Furthermore, the proposed formulation shows convincing values of performance indices (Tables 1 and 2). Our implementation outperforms in all cases of the input scenes—higher values of PSNR and MSSIM. One may, however, argue about the marginal deviation of the numerical results between the traditional Perona–Malik and ours. Nevertheless, the proposed approach eliminates the necessity to tune critical parameters (shape-defining constant and regularization parameter) to achieve optimal results.

4. Conclusion

The current work has established a framework to automate the PM diffusion model. More specifically, we have redefined the shape-defining and regularizing parameters such that they spatially update their values to ensure convexity of the corresponding PM potential. The new formulation eliminates the need to manually tune the shape-defining constant, a process that unnecessarily consumes time, and also guarantees convergence and stability. Previous variants of the PM model have largely invested on improving the diffusion kernel without emphasizing on the critical roles played by the shape-defining parameter. Our major concern in this paper was to automate the classical PM model by redefining the shape-defining constant. Hopefully, the automatic PM model presented in this paper will provide important research avenues in fields that demand real-time computing.

Competing interests

The authors declare that they have no competing interests to disclose.

Acknowledgements

This work is not funded by any organization.

References

[1] Z. Guo, J. Sun, D. Zhang, B. Wu, Adaptive Perona–Malik model based on the variable exponent for image denoising, IEEE Trans. Image Process. 21 (2012) 958–967.
[2] E. Cuesta, M. Kirane, S.A. Malik, Image structure preserving denoising using generalized fractional time integrals, Signal Process. 92 (2012) 553–563.
[3] H. Li, P. Fan, M.K. Khan, Context-adaptive anisotropic diffusion for image denoising, Electron. Lett. 48 (2012) 827–829.
[4] A. Atlas, F. Karami, D. Meskine, The Perona–Malik inequality and application to image denoising, Nonlinear Anal., Real World Appl. 18 (2014) 57–68.
[5] C. Tsiotsios, M. Petrou, On the choice of the parameters for anisotropic diffusion in image processing, Pattern Recognit. 46 (2013) 1369–1381.
[6] J. Yuan, Improved anisotropic diffusion equation based on new nonlocal information scheme for image denoising, IET Comput. Vis. 9 (2015) 864–870.
[7] S.K. Jain, R.K. Ray, A. Bhavsar, A comparative study of iterative solvers for image de-noising, in: Proceedings of the 3rd International Conference on Frontiers of Intelligent Computing: Theory and Applications (FICTA), Springer, 2014, pp. 307–314.
[8] B. Wu, E.A. Ogada, J. Sun, Z. Guo, A total variation model based on the strictly convex modification for image denoising, in: Abstract and Applied Analysis, vol. 2014, Hindawi Publishing Corporation, 2014.
[9] E.A. Ogada, Z. Guo, B. Wu, An alternative variational framework for image denoising, in: Abstract and Applied Analysis, vol. 2014, Hindawi Publishing Corporation, 2014.
[10] L.I. Rudin, S. Osher, E. Fatemi, Nonlinear total variation based noise removal algorithms, Physica D 60 (1992) 259–268.
[11] P. Perona, J. Malik, Scale-space and edge detection using anisotropic diffusion, IEEE Trans. Pattern Anal. Mach. Intell. 12 (1990) 629–639.
[12] M. Paulinas, A. Ušinskas, A survey of genetic algorithms applications for image enhancement and segmentation, Inf. Technol. Control 36 (2015).
[13] J. Gangadharan, S. Mani, K. Kutty, Low Light Image Enhancement Using Color Transfer, Technical Report, SAE Technical Paper, 2015.
[14] R. Roy, A.P. Kumar, A.K. Yadav, et al., Histogram equalization for image enhancement using kidney ultrasound images, J. Image Process. Pattern Recognit. Prog. 2 (2015) 20–26.
[15] S.R.P. Pavani, System and method for spatio video image enhancement, 2015, US Patent App. 14/603,996.
[16] C. Chen, H. Liang, S. Zhao, Z. Lyu, M. Sarem, A novel multi-image super-resolution reconstruction method using anisotropic fractional order adaptive norm, Vis. Comput. (2014) 1–15.

[17] D.P. Kouri, E.A. Shields, Efficient multiframe super-resolution for imagery with lateral shifts, Appl. Opt. 53 (2014) F1–F9.
[18] B.N. Narayanan, R.C. Hardie, E.J. Balster, Multiframe adaptive Wiener filter super-resolution with jpeg2000-compressed images, EURASIP J. Adv. Signal Process. 2014 (2014) 1–18.
[19] X. Li, Y. Hu, X. Gao, D. Tao, B. Ning, A multi-frame image super-resolution method, Signal Process. 90 (2010) 405–414.
[20] L. Zhang, Q. Yuan, H. Shen, P. Li, Multiframe image super-resolution adapted with local spatial information, J. Opt. Soc. Am. A 28 (2011) 381–390.
[21] X. Zeng, L. Yang, A robust multiframe super-resolution algorithm based on half-quadratic estimation with modified btv regularization, Digit. Signal Process. 23 (2013) 98–109.
[22] L. Pickup, S. Roberts, A. Zisserman, D. Capel, Multiframe super-resolution from a Bayesian perspective, Super-Resolution Imaging (2010) 247.
[23] B. Maiseli, O. Elisha, J. Mei, H. Gao, Edge preservation image enlargement and enhancement method based on the adaptive Perona–Malik non-linear diffusion model, IET Image Process. 8 (12) (2014) 753–760.
[24] S. Farsiu, M.D. Robinson, M. Elad, P. Milanfar, Fast and robust multiframe super resolution, IEEE Trans. Image Process. 13 (2004) 1327–1344.
[25] B. Maiseli, C. Wu, J. Mei, Q. Liu, H. Gao, A robust super-resolution method with improved high-frequency components estimation and aliasing correction capabilities, J. Franklin Inst. 351 (2014) 513–527.
[26] R.M. Bahy, G.I. Salama, T.A. Mahmoud, Adaptive regularization-based super resolution reconstruction technique for multi-focus low-resolution images, Signal Process. 103 (2014) 155–167.
[27] S. Villena, M. Vega, S.D. Babacan, R. Molina, A.K. Katsaggelos, Bayesian combination of sparse and non-sparse priors in image super resolution, Digit. Signal Process. 23 (2013) 530–541.
[28] D. Kim, H. Byun, Regularization based super-resolution image processing algorithm using edge-adaptive non-local means filter, in: Proceedings of the 7th International Conference on Ubiquitous Information Management and Communication, ACM, 2013, p. 78.
[29] C. Guillemot, O. Le Meur, Image inpainting: overview and recent advances, IEEE Signal Process. Mag. 31 (2014) 127–144.
[30] H.M. Patel, H.L. Desai, A review on design, implementation and performance analysis of the image inpainting technique based on tv model, Int. J. Eng. Dev. Res. 2 (2014) 191–195.
[31] M. Imtiyaz, A. Kumar, G. Sreenivasulu, Inpainting an image based on enhanced resolution, Int. J. Comput. Appl. Technol. 6 (2015) 23–26.
[32] X.F. Yin, J.M. Duan, Z.K. Pan, W.B. Wei, G.D. Wang, Nonlocal tv-l1 inpainting model and its augmented lagrangian algorithm, in: Applied Mechanics and Materials, vol. 644, Trans Tech Publ, 2014, pp. 4630–4636.
[33] V. Caselles, Variational models for image inpainting, in: European Congress of Mathematics, Kraków, 2–7 July 2012, pp. 227–242.
[34] W. Yu, S. Heber, T. Pock, Learning reaction–diffusion models for image inpainting, in: Pattern Recognition, Springer, 2015, pp. 356–367.
[35] Z. Qin, D. Goldfarb, S. Ma, An alternating direction method for total variation denoising, Optim. Methods Softw. (2014) 1–22.
[36] D. Chen, Y. Chen, D. Xue, Fractional-order total variation image denoising based on proximity algorithm, Appl. Math. Comput. 257 (2015) 537–545.
[37] X. Liu, L. Huang, A new nonlocal total variation regularization algorithm for image denoising, Math. Comput. Simul. 97 (2014) 224–233.
[38] P. Sharma, K. Khan, K. Ahmad, Image denoising using local contrast and adaptive mean in wavelet transform domain, Int. J. Wavelets Multiresolut. Inf. Process. 12 (2014) 1450038.
[39] W. Cheng, K. Hirakawa, Minimum risk wavelet shrinkage operator for Poisson image denoising, IEEE Trans. Image Process. 24 (2015) 1660–1671.
[40] N. Remenyi, O. Nicolis, G. Nason, B. Vidakovic, Image denoising with 2d scale-mixing complex wavelet transforms, IEEE Trans. Image Process. 23 (2014) 5165–5174.
[41] B. Rasti, J.R. Sveinsson, M.O. Ulfarsson, J.A. Benediktsson, Hyperspectral image denoising using first order spectral roughness penalty in wavelet domain, IEEE J. Sel. Top. Appl. Earth Obs. Remote Sens. 7 (2014) 2458–2467.
[42] F. Liu, J. Liu, Anisotropic diffusion for image denoising based on diffusion tensors, J. Vis. Commun. Image Represent. 23 (2012) 516–521.
[43] A. Maleki, M. Narayan, R.G. Baraniuk, Anisotropic nonlocal means denoising, Appl. Comput. Harmon. Anal. 35 (2013) 452–482.
[44] J. Weickert, A review of nonlinear diffusion filtering, in: Scale-Space Theory in Computer Vision, Springer, 1997, pp. 1–28.
[45] S. Kichenassamy, The Perona–Malik paradox, SIAM J. Appl. Math. 57 (1997) 1328–1342.
[46] P. Guidotti, A backward–forward regularization of the Perona–Malik equation, J. Differ. Equ. 252 (2012) 3226–3244.
[47] J. Canny, A computational approach to edge detection, IEEE Trans. Pattern Anal. Mach. Intell. (1986) 679–698.
[48] J. Weickert, B.T.H. Romeny, M. Viergever, et al., Efficient and reliable schemes for nonlinear diffusion filtering, IEEE Trans. Image Process. 7 (1998) 398–410.
[49] R. Courant, K. Friedrichs, H. Lewy, On the partial difference equations of mathematical physics, IBM J. Res. Dev. 11 (1967) 215–234.
[50] Z. Wang, A.C. Bovik, Mean squared error: love it or leave it? A new look at signal fidelity measures, IEEE Signal Process. Mag. 26 (2009) 98–117.
[51] Z. Wang, A.C. Bovik, H.R. Sheikh, E.P. Simoncelli, Image quality assessment: from error visibility to structural similarity, IEEE Trans. Image Process. 13 (2004) 600–612.